Synchronization in chaotic Hamiltonian systems and a geophysical application

A. Hannachi
Atmospheric, Oceanic and Planetary Physics, Clarendon Laboratory, Parks Road, Oxford OX1 3PU, United Kingdom
(Received 25 January 1999)

This paper addresses the question of the rate of synchronization of two identical systems as a function of the inserting time interval Δt between inserted variables of the driving system in the role of the same variables of the driven system in a simplified Hamiltonian system and its application to a simplified geophysical model. We start by analyzing the synchronization in a simplified two-degree Hamiltonian system. The synchronization rate turns out to be a decreasing function of the inserting time interval Δt up to a certain limit Δt_o where the process reverses and the synchronization rate becomes slower as the inserting frequency decreases. The key point of the analysis uses a second-order Taylor expansion of the system resolvent which indicates that synchronization rate is basically of order $O(\Delta t^2)$ for small Δt. The study is then extended to include a simplified geophysical system. A nonlinear one-dimensional shallow-water model on a periodic domain meant to represent a latitudinal circle around 45 °N is used. It is found that when the zonal wind is inserted, the maximum synchronization rate is obtained when the inserting time interval is approximately 4 h. When the meridional wind is inserted, it is obtained at slightly less than 4 h. It is shown, in particular, that the synchronization rate depends on the latitude (or the Coriolis parameter). A low-order simplified dynamical system derived from the one-dimensional shallow-water model is used to show that this optimum time interval Δt_o when the zonal wind and the geopotential, for example, are inserted varies approximately as $\sqrt{2}/2\Omega \sin\varphi$ to accuracy $O(\Delta t^3)$. Analyses performed with a linear version of the shallow-water model reveal that this latter can be used to explain the observed convergence behavior in the nonlinear model. The only point is the choice of the stationary state for linearization purposes. It is then suggested that in more complicated geophysical systems, the closest stationary state to the climatology can be used to estimate the crossover point Δt_o. [S1063-651X(99)08507-4]

PACS number(s): 05.45.−a, 02.30.Jr, 92.60.−e

I. INTRODUCTION

Synchronization is commonly observed in low-order chaotic and, to a lesser extent, in extended systems. Advances in computing power have also led to a better understanding of the behavior of these systems regarding synchronization. A familiar way to obtain synchronization is through coupling of two (or more) identical systems in a drive/response manner as performed in [1]. As pointed out in the next section, the same synchronization can be obtained by periodically inserting (or updating) one (or more) system variables from the driving trajectory (or control run), obtained by running the model forward in time, into the role of the same variables of the driven (or response) system that is integrated with a different initial condition keeping the remaining system variables unchanged.

Since its introduction in low-order chaotic systems [1,2], synchronization has gone through a wide range of application in physical sciences. While Pecora and Caroll [1], for example, introduced it in connection with low-order chaotic models and applied it to an electronic chaotic circuit, others suggested its application to filtering, by deducing the state of a chaotic system from a limited sample of observations [3], communications [4], and system identification [5]. The suggestion regarding the application of synchronization to fluids [2] plus its observed robustness in chaotic systems vis-à-vis the presence of noise [3,5] constitute a good grounding for geophysical application, particularly in atmospheric sciences regarding, for example, prediction. Duane [6], who studied the phenomenon in connection with teleconnection in meteorology, observed a partial synchronization between the two hemispheres; the northern hemispheric flow regimes tend to partially synchronize with those of the southern hemisphere.

As far as fluids and therefore meteorology are concerned, the issue is of great importance. In fact, it is well known that the current meteorological and oceanographical observational network has been much improved lately regarding the quality as well as the quantity of data. For example, sea surface height data as measured by satellite are available with a wide spatial and temporal cover at very high accuracy. Although this coverage is far from satisfactory in the sense that only a limited number of independent atmospheric or oceanic variables are observed, the subset of the observed meteorological variables turns out to be very useful in predicting the future state of the ocean/atmosphere system using numerical weather prediction models in a way similar to that of synchronization.

Although the terminology is new in physics, the method has been applied in meteorology since the early 1970s and usually known as periodic updating [7–9]. For example, Charney, Halem, and Jastrow [7] applied an updating operation using a simplified model of the atmosphere. They showed that, when the temperature of the driving system is inserted in the role of the same variable of the driven system, the greatest reduction of the error variance, defined as the Euclidean distance between the states of the two systems, was achieved when the temperature is inserted every 12 h. They pointed out that a more frequent insertion of these thermal impulses seemed to give rise to inertio-gravity oscillations which prevented the dissipative forces from adjusting

the wind field to the temperature field. On the other hand, investigations from a simplified one-dimensional (1D) linear shallow-water model indicate that the inserting interval should be greater than the decay time of inertio-gravity waves in order to avoid data redundancy [8]. Other investigators observed that the synchronization was achieved faster for some larger inserting time intervals [10]. The inserting time interval and also the observation error along with contributions from other sources can have a great impact on the degradation of the synchronization [5,6,9].

The question of the rate of synchronization as a function of the updating (inserting) frequency has been addressed in [11] using low-order chaotic systems. Here we investigate the same question and its application to simplified geophysical models. More precisely, we address the question of how often to update, or insert, in order that the two systems get synchronized as quickly as possible. We use for this purpose a low-order chaotic Hamiltonian system as well as a simplified geophysical model and perform a synchronization experiment as in [1], namely, two identical systems in drive/driven manner using (periodic) insertion of variables from the driving signal in the role of the same variables of the driven system. Specifically, the dynamical model is first run with a given initial condition for a long period of time. This driving trajectory, or control run, is saved and is used as perfect observations. The model is then rerun with a different initial condition, to yield the driven system, and periodically updated with the same subset of variables taken from the driving trajectory, ignoring the correlation between observed and unobserved variables, until the driven trajectory eventually converges toward the driving trajectory. Obviously, for large systems the two runs can be performed simultaneously.

In Sec. II, we provide theoretical and experimental analyses of the rate of synchronization as a function of the inserting time interval in a simple two-degree Hamiltonian system. Experimental analysis is extended in Sec. III to include a simplified nonlinear 1D shallow-water model. Analytical analysis is then developed in Sec. IV by deriving a simplified low-order dynamical system from the shallow-water model to confirm the experimental results of Sec. III. In Sec. V, a comparison with analyses from a linear version of the shallow-water model is performed. Summary and conclusion are presented in the last section.

II. SYNCHRONIZED CHAOS IN A SIMPLE HAMILTONIAN SYSTEM

A. Perturbation of dynamical systems by updating process

As pointed out earlier, a similar approach to synchronization by direct coupling between two identical systems as performed originally by [1,2] can be achieved through a direct insertion of a subset of variables from the driving system in the role of the same variables in the driven system. In this operation the model is run first and the trajectory saved each time step. The same model is then rerun with different initial condition, the chosen variables periodically inserted, and the distance between the two system states computed. In fact, consider a general autonomous m-dimensional dynamical system

$$\frac{d\mathbf{X}}{dt}=\mathbf{F}(\mathbf{X}) \tag{1}$$

and denote by $\mathbf{X}^T=(\mathbf{X}_o^T,\mathbf{X}_u^T)$ where $\mathbf{X}_o$ stands for the driving, or observed, variables hence subscript o, while $\mathbf{X}_u$ represents the remaining or ''unobserved'' variables and the superscript T stands for the transpose operator. Accordingly, Eq. (1) can be split into two subsystems as

$$\begin{aligned}\dot{\mathbf{X}}_o&=\mathbf{F}_o(\mathbf{X}),\\ \dot{\mathbf{X}}_u&=\mathbf{F}_u(\mathbf{X}),\end{aligned} \tag{2}$$

where $\mathbf{F}^T=(\mathbf{F}_o^T,\mathbf{F}_u^T)$ is the corresponding split of $\mathbf{F}$. As in [1,2], the augmented system is

$$\begin{aligned}\dot{\mathbf{X}}_o&=\mathbf{F}_o(\mathbf{X}),\\ \dot{\mathbf{X}}_u&=\mathbf{F}_u(\mathbf{X}),\\ \mathbf{Y}_o&=\mathbf{X}_o,\\ \dot{\mathbf{Y}}_u&=\mathbf{F}_u(\mathbf{Y}),\end{aligned} \tag{3}$$

where $\mathbf{Y}^T=(\mathbf{Y}_o^T,\mathbf{Y}_u^T)$ and $\mathbf{Y}_u$ represents the responding variables. The integration of Eq. (3) gives therefore the same result as the mentioned inserting procedure, obtained by running Eq. (1) twice, when the insertion is performed every time step δt. It is of course cheaper to run Eq. (3) than running Eq. (1) twice as far as synchronization with identical systems is concerned. However, for our purpose of inserting variables every time interval Δt we need in fact to integrate Eq. (1) twice. The reason for this, as detailed below, can be understood after writing Eq. (1) in a discretized form, or as a map, $\mathbf{X}^{i+1}=\mathbf{f}(\mathbf{X}^i)$. Now for a given $N\geqslant 1$ we write our new coupled system as

$$\begin{aligned}\mathbf{X}_o^{i+1}&=\mathbf{f}_o(\mathbf{X}^i),\\ \mathbf{X}_u^{i+1}&=\mathbf{f}_u(\mathbf{X}^i),\\ \mathbf{Y}_o^{i+1}&=\xi_i\mathbf{X}_o^{i+1}+(1-\xi_i)\mathbf{f}_o(\mathbf{Y}^i),\\ \mathbf{Y}_u^{i+1}&=\mathbf{f}_u(\mathbf{Y}^i),\end{aligned} \tag{4}$$

where the function ξ_i is given by

$$\xi_i=\begin{cases}1 & \text{if } 0\equiv i \pmod N\\ 0 & \text{otherwise.}\end{cases}$$

The inserting procedure for each N steps is now straightforward from Eq. (4). Here N is meant to represent the length of the inserting time interval Δt given in number of time steps, i.e., $\Delta t=N\delta t$. Note also from Eq. (4) that the usual coupling [Eq. (3)] [1,2] is obtained for the particular case $N=1$.

During the insertion procedure, and in the limit of small changes, the trajectory of Eq. (1) is being periodically disturbed. Since the driving/driven systems are identical, the changes in the variable $\mathbf{X}$ at the time of insertion are

$$\delta\mathbf{X}^T=(\delta\mathbf{X}_o^T,\delta\mathbf{X}_u^T)=(\mathbf{O},\delta\mathbf{X}_u^T). \tag{5}$$

Now a small perturbation $\delta\mathbf{X}_0$ superimposed onto Eq. (1) at time $t=0$ will evolve according to

$$\frac{d\,\delta\mathbf{X}}{dt}=\mathbf{F}'(\mathbf{X}(t))\,\delta\mathbf{X}, \tag{6}$$

where $\mathbf{F}'(\mathbf{X}(t))=(\partial\mathbf{F}/\partial\mathbf{X})(\mathbf{X}(t))$ is the Jacobian of $\mathbf{F}$ at $\mathbf{X}(t)$. The solution to Eq. (6) is given by

$$\delta\mathbf{X}(t)=\mathbf{R}(t,t_0)\,\delta\mathbf{X}(t_0), \tag{7}$$

where $\mathbf{R}(t,t_0)$ is the resolvent (or propagator) of Eq. (6). It can be easily verified that this latter satisfies the following equations:

$$\frac{\partial}{\partial t}\mathbf{R}(t,t_0)=\mathbf{F}'(\mathbf{X}(t))\mathbf{R}(t,t_0),\quad \text{and } \mathbf{R}(t,t)=\mathbf{I}_m\quad \forall t,t_0 \tag{8}$$

where $\mathbf{I}_m$ is the m-dimensional identity matrix. The propagator $\mathbf{R}(t,t_0)$ cannot be explicitly computed for general, and even simple, nonlinear systems. However, for small Δt, we can use the Taylor expansion:

$$\mathbf{R}(t_0+\Delta t,t_0)=\mathbf{I}_m+\Delta t\,\frac{\partial}{\partial t}\mathbf{R}(t,t_0)\big|_{t=t_0}+\cdots + \frac{\Delta t^n}{n!}\,\frac{\partial^n}{\partial t^n}\mathbf{R}(t,t_0)\big|_{t=t_0}+\mathbf{O}(\Delta t^{n+1}). \tag{9}$$

To accuracy $O(\Delta t^3)$, the previous expansion, along with Eq. (8), boil down to

$$\mathbf{R}(t_0+\Delta t,t_0)=\mathbf{I}_m+\Delta t\mathbf{F}'(\mathbf{X}(t_0)) + \frac{\Delta t^2}{2}[\dot{\mathbf{F}}'(\mathbf{X}(t_0))+\mathbf{F}'^2(\mathbf{X}(t_0))]+\mathbf{O}(\Delta t^3). \tag{10}$$

In Eq. (10), t_0 is chosen arbitrarily as initial time but it can be any time t_k so that the coefficients of Δt and Δt^2 in the right hand side of Eq. (10) are functions of time t_k. The case where these coefficients are time independent will be addressed in Sec. V. According to Eq. (2), the propagator $\mathbf{R}$ is also split into four subpropagators $\mathbf{R}_{oo}$, $\mathbf{R}_{ou}$, $\mathbf{R}_{uo}$, and $\mathbf{R}_{uu}$. Using Eqs. (5) and (7) we get the recurrence relationship;

$$\delta\mathbf{X}_u(t_k)=\mathbf{R}_{uu}(t_k,t_{k-1})\,\delta\mathbf{X}_u(t_{k-1}). \tag{11}$$

The matrix $\mathbf{R}_{uu}(t_k,t_{k-1})$ is referred to as the amplification matrix hereafter. The two systems therefore synchronize, or the sequence of Eq. (11) is said to be convergent, if $\delta\mathbf{X}_u(t)$ [or similarly $\delta\mathbf{X}(t)$] tends to zero when t tends to infinity for all initial values of $\delta\mathbf{X}_0$. The process is then convergent, for small $\Delta t_k=t_k-t_{k-1}$, if and only if $\mathbf{A}_n=\Pi_{k=1}^{n}\mathbf{R}_{uu}(t_{n-k+1},t_{n-k})$ converges to the null matrix when n goes to infinity.

If $\rho_n=\rho(\mathbf{A}_n)$ denotes the spectral radius of $\mathbf{A}_n$, then a necessary condition (and in general sufficient only for normal matrices) for the process to converge is that $\rho_n\to 0$ when $n\to\infty$. Note also that while, in general, the resolvent matrices are not normal, convergence does occur in the numerical experiments when the necessary condition is satisfied.

B. Application to a simple Hamiltonian system

Although Hamiltonian systems constitute a small subset of the conservative systems, they still hold a considerable position among geophysicists' topics. It is in fact known that geophysical (atmosphere plus ocean) systems behave very much like Hamiltonian systems, especially over short periods or when dissipation and forcing are weak. In fact, a Hamiltonian formulation of geophysical fluid dynamics can be found in [13].

For convenience and prior to using a simplified geophysical model, we consider here the same system used in [11], namely, the Hénon and Heiles two-degree Hamiltonian system [14] with potential U and Hamiltonian H:

$$U(x,y)=\tfrac{1}{2}(x^2+y^2+2x^2y-\tfrac{2}{3}y^3)\quad \text{and}$$

$$H=\tfrac{1}{2}(x^2+y^2+p^2+q^2)+x^2y-\tfrac{1}{3}y^3, \tag{12}$$

where (x,y) is the particle position and $(p,q)=(\dot{x},\dot{y})$ represents the velocity of the particle in the potential well U. The equations of motion are given by

$$\frac{d\mathbf{X}}{dt}=\boldsymbol{\mathcal{I}}\cdot\boldsymbol{\nabla}H=\mathbf{F}(\mathbf{X}), \tag{13}$$

where

$$\boldsymbol{\mathcal{I}}=\begin{pmatrix}\mathbf{O} & \mathbf{I}_2\\ -\mathbf{I}_2 & \mathbf{O}\end{pmatrix},$$

where $\mathbf{O}$ and $\mathbf{I}_2$ are 2×2 null and identity matrices, respectively, and $\mathbf{X}=(x,y,p,q)^T$ and $\mathbf{F}(\mathbf{X})=(p,q,-x-2xy,-y-x^2+y^2)^T$. Any system trajectory is confined to a constant energy level given by the value of H, and the behavior of the system phase space depends on this level where regularity is observed at low levels while irregularity and chaotic behavior are characteristics of high energy levels [11,12].

For this system we have

$$\mathbf{F}'(\mathbf{X}(t))=\begin{pmatrix}\mathbf{O} & \mathbf{I}_2\\ \mathbf{A}_2 & \mathbf{O}\end{pmatrix}$$

and

$$\dot{\mathbf{F}}'(\mathbf{X}(t))+\mathbf{F}'^2(\mathbf{X}(t))=\begin{pmatrix}\mathbf{A}_2 & \mathbf{O}\\ \mathbf{B}_2 & \mathbf{A}_2\end{pmatrix}, \tag{14}$$

where

$$\mathbf{A}_2=\begin{pmatrix}-1-2y & -2x\\ -2x & -1+2y\end{pmatrix}\quad \text{and}\quad \mathbf{B}_2=\begin{pmatrix}-2q & -2p\\ -2p & 2q\end{pmatrix}.$$

It is clear from Eqs. (14) and (10) that when the position variables (x,y) or the momentum variables (p,q) are inserted (in the driven system), the coefficient of Δt in $\mathbf{R}_{uu}$ is null. This is true for all Hamiltonian systems deriving from a potential, i.e., both the amplification matrix $\mathbf{R}_{uu}$ and the syn-

chronization rate are $O(\Delta t^2)$ for small Δt. For this case, the amplification matrix $\mathbf{R}_{uu}^{(k)}=\mathbf{R}_{uu}(t_k,t_{k-1})$ is

$$\mathbf{R}_{uu}^{(k)}=\mathbf{I}_2+\frac{\Delta t^2}{2}\mathbf{A}^2 =\begin{pmatrix} 1-\frac{\Delta t^2}{2}(1+2y_k) & -\Delta t^2 x_k \\ -\Delta t^2 x_k & 1-\frac{\Delta t^2}{2}(1-2y_k) \end{pmatrix}, \tag{15}$$

where $(x_k,y_k,p_k,q_k)=(x(t_k),y(t_k),p(t_k),q(t_k))$.

In the case where $\mathbf{X}_o=(x,q)^T$ we have

$$\mathbf{R}_{uu}(t_k,t_{k-1})=\begin{pmatrix} 1-\frac{\Delta t^2}{2}(1+2y_k) & 0 \\ -2x_k\Delta t-p_k\Delta t^2 & 1-\frac{\Delta t^2}{2}(1-2y_k) \end{pmatrix} \tag{16}$$

and for $\mathbf{X}_o=(y,p)^T$, the diagonal elements of Eq. (16) should be interchanged. For both cases, the spectral radius ρ_n of $\mathbf{A}_n$ is explicitly given by

$$\rho_n=\max\left(\prod_{k=1}^{n}\left|1-\frac{\Delta t^2}{2}(1+2y_k)\right|, \prod_{k=1}^{n}\left|1-\frac{\Delta t^2}{2}(1-2y_k)\right|\right). \tag{17}$$

Appendix A shows that for small Δt, ρ_n goes to zero as n goes to infinity and that $\rho_n(\Delta t)$ is a decreasing function of Δt for $\Delta t<\sqrt{2}$, i.e.,

$$\rho_n(\Delta_2 t)\leqslant\rho_n(\Delta_1 t) \quad \text{for } \Delta_1 t\leqslant\Delta_2 t<\sqrt{2}, \tag{18}$$

where $\Delta_1 t$ and $\Delta_2 t$ are two inserting (updating) time intervals. It is also shown (Appendix A) that for two different inserting cycles $n_2\leqslant n_1$ for which $n_1\Delta_1 t=n_2\Delta_2 t=\sigma$, that is, the $(n_2,\Delta_2 t)$ cycle inserts less data than $(n_1,\Delta_1 t)$, we still have

$$\rho_{n_2}(\Delta_2 t)\leqslant\rho_{n_1}(\Delta_1 t). \tag{19}$$

As an application a driving trajectory is obtained by numerically integrating Eq. (1) forward in time using a fourth-order Runge-Kutta scheme in order to conserve the energy H with time step $\delta t=5\times10^{-3}$. Any trajectory is defined by its initial condition, (x_0,y_0,q_0), for example, and its energy level H which determines the remaining variable. The inserting time interval is taken to be a multiple of the time step, i.e., $\Delta t=N\delta t$. As a measure of synchronization we choose the squared error (SQE), i.e., the squared Euclidean distance, between the states of the two (driving and driven) systems. In Fig. 1 we display the squared error as a function of time for different values of N when (x,q) [Fig. 1(a)] and (x,y) [Fig. 1(b)] are inserted. The driving trajectory used in Fig. 1 is defined by $(x_0,y_0,q_0)=(0,0.1,0.2)$ at $H=0.165$ and corresponds to a chaotic trajectory [11]. Figure 1 shows clearly

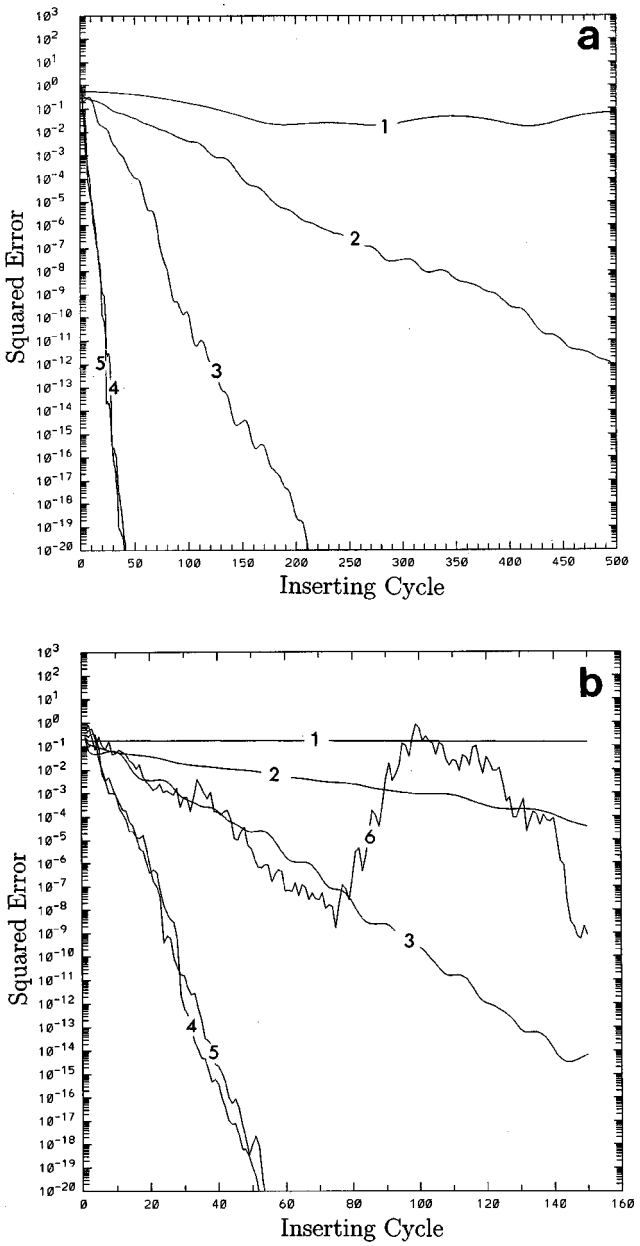

FIG. 1. The squared error (SQE) vs the number of inserting cycle during the insertion of x and q (a) for different inserting time intervals Δt fixed to $5\delta t$ (curve 1), $50\delta t$ (curve 2), $100\delta t$ (curve 3), $250\delta t$ (curve 4), and $300\delta t$ (curve 5), and when x and y are inserted (b) with the same inserting time intervals with one more Δt fixed to $450\delta t$ (curve 6). Note that curves 4 and 5 in panel (a) are hardly distinguishable.

that the synchronization (or convergence) is faster for larger Δt up to a maximum value Δt_o. Note, however, from Fig. 1(a) that curves 4 and 5 are hardly distinguishable. This implies that $\Delta t_o\approx(200-300)\delta t\sim1.3$, in close agreement with the theoretical value $\sqrt{2}$ (Appendix A). When $\mathbf{X}_o=(x,y)$ or (p,q) and the amplification matrix is given by Eq. (15), Fig. 1(b) still shows the same behavior and where, in order to show slower convergence or actual divergence for larger intervals Δt, one more curve, corresponding to $N=450$ (curve 6), is added. However, due to the position of curve 4 with respect to curve 5 (to its left), Δt_o is closer to $250\delta t$ than to $300\delta t$. An approximation to the value of Δt_o can be read

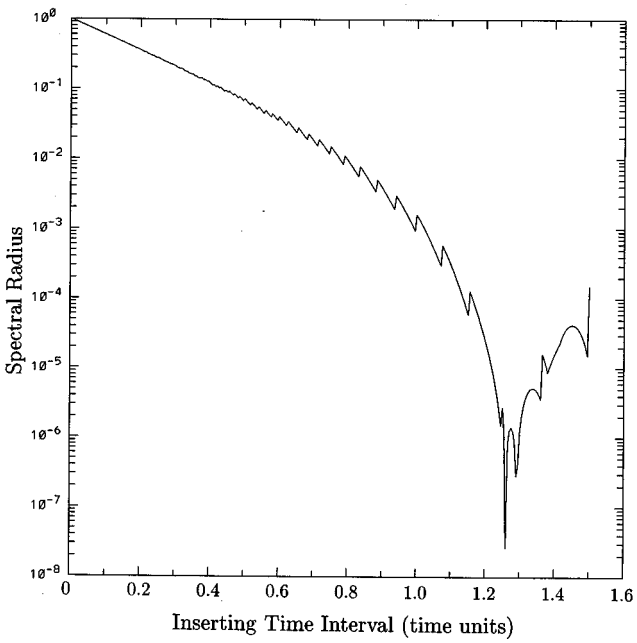

FIG. 2. The spectral radius ρ_n of $\mathbf{A}_n$ vs the inserting interval Δt when the amplification matrix $\mathbf{R}_{uu}^{(n)}$ is given by Eq. (16), i.e., when (x,q) are inserted. Notice the interval Δt_o around 1.3 beyond which the convergence rate is no longer increasing with Δt. The small bursts are certainly due to the nonsmoothness of the spectral radius. Same driving trajectory as in Fig. 1.

from Fig. 2 which shows the variation of the spectral radius (i.e., convergence, or synchronization, rate) ρ_n of $\mathbf{A}_n$ with Δt when (x,q) [Fig. 1(a)] or (y,p) are inserted indicating that Δt_o is near 1.3. Notice, however, the existence of local minima around the global minimum leading to the cluster of curves obtained when $\Delta t=(200-300)\delta t$ (Fig. 1). More details on the determination of Δt_o can be found in [11], where a third-order Taylor expansion of the resolvent was used.

III. APPLICATION TO A SIMPLIFIED GEOPHYSICAL MODEL

A. Simplified primitive equations model

As pointed out in the Introduction, in numerical weather prediction only some, not all, meteorological variables are observed. The combination of this subset of observations with the numerical model in a driving/response manner makes the connection with synchronization straightforward. This combination is generally based on the assumption that the observations are compatible with the model. The atmospheric system is modeled by nonlinear partial differential equations based on the momentum, energy, continuity, and the state equations forming altogether the so-called primitive equations. When these equations are projected onto a specified basis as in spectral methods, and a cutoff applied, the system becomes equivalent to a finite dynamical system where the previous analytical techniques can be applied.

As a simplified version of the primitive equations we consider a 1D nonlinear shallow-water model (SWM) over a periodic domain with circumference l, representing a latitudinal circle around 45 °N. Roughly speaking, the general shallow-water equations are used to model the motion of a fluid with free upper boundary. These equations were shown to provide a reasonable approximation to the circulation of the troposphere, the lower part of the atmosphere [15], and also to the dynamics of the upper ocean [16]. The 1D equations, written in Cartesian coordinates for an f plane, are the following:

$$\begin{aligned} u_t+uu_x+\phi_x-fv&=\nu u_{xx}+F_u,\\ v_t+uv_x+fu&=\nu v_{xx}+F_v,\\ \phi_t+u\phi_x+\phi u_x&=0, \end{aligned} \tag{20}$$

where u and v are the zonal and meridional winds, respectively, $\phi=gh$ and is called the geopotential (g is the gravity and h is the fluid height), f is the Coriolis parameter, ν is the dissipation rate (viscosity), and F_u and F_v are constant forcing. Time and space derivatives are indicated by the subscripts t and x, respectively. The first two equations represent Newton's second law of motion on a rotating frame while the last one is derived from the continuity equation combined with the lower and free surface boundary conditions [17]. Normally for our analysis, we consider the nondissipative and unforced version of Eq. (20) which is nondimensionalized using $T=f^{-1}$ and $L=10^3$ km as units of time and length, respectively (synoptic scales), and to keep the wind speed within the range of observed values in the troposphere u and v are nondimensionalized by $U_0=20\,\mathrm{ms}^{-1}$, and ϕ by $\Phi_0=10^4\,\mathrm{m}^2\,\mathrm{s}^{-2}$ corresponding to an internal mode. The nondimensionalized unforced and nondissipative 1D shallow-water model reads

$$\begin{aligned} u_t+R_ouu_x+F_o\phi_x-v&=0,\\ v_t+R_ouv_x+u&=0,\\ \phi_t+R_o(u\phi_x+\phi u_x)&=0, \end{aligned} \tag{21}$$

where $R_o=U_0/Lf$ is the Rossby number, and $F_o=\Phi_0/U_0Lf$. At midlatitude, $\varphi=45\,°\mathrm{N}$, $R_o=0.2$, and $F_o=5$. The energy equation derived from Eq. (21) can be written as

$$\frac{\partial}{\partial t}\left[\phi\left(\frac{R_o}{F_o}V^2+\phi\right)\right]+R_o\frac{\partial}{\partial x}\left[\phi u\left(\frac{R_o}{F_o}V^2+\phi\right)+u\phi^2\right]=0, \tag{22}$$

where $V^2=u^2+v^2$, and the total energy $E=\int_{\mathrm{domain}}\phi[(R_o/F_o)V^2+\phi]dx$, is therefore conserved.

Sasaki [18] used a similar one-dimensional f-plane shallow-water model to study a problem of initialization using a variational adjustment method of the field variables in order to have a best initial guess for prediction purposes. The one-dimensional model is restrictive as to dynamical process representation because all variables are uniform in the y direction and the zonal component of wind can represent only ageostrophic inertio-gravity waves although the zonal current should be largely geostrophic in reality. However, the model is very useful, at least qualitatively, to address and understand issues that may be difficult to address with more complicated models.

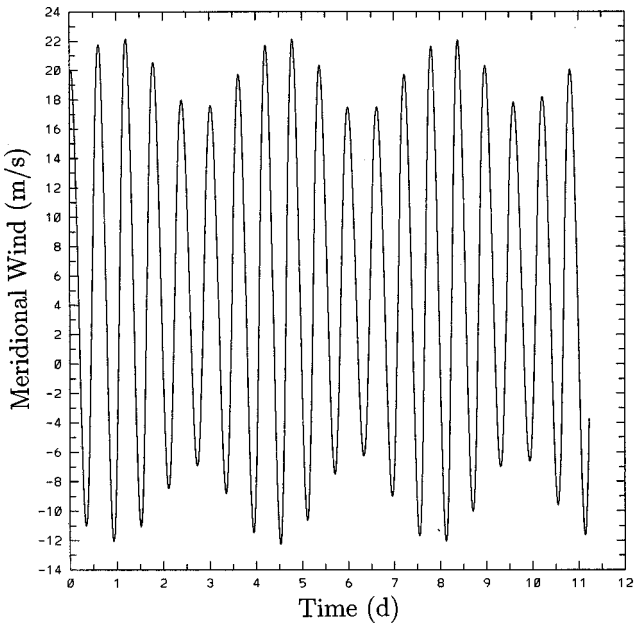

FIG. 3. The meridional wind v at grid point 20 as a function of time when the initial conditions are given by $u_0(x)=\sin(6\pi xL/l)$, $v_0(x)=\cos(6\pi xL/l)$, and $\phi_0=1$. The numerical scheme is a fourth-order Runge-Kutta scheme with (nondimensional) time step $\delta t=10^{-2}$ (corresponding to 1.7 min).

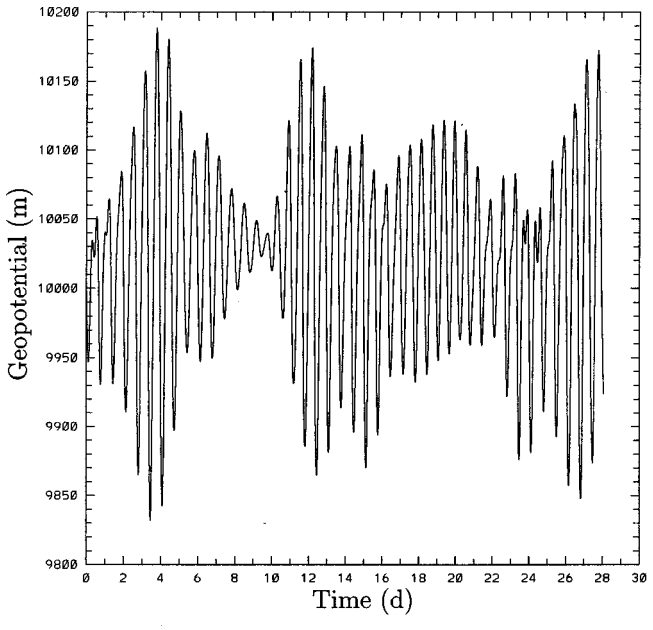

FIG. 4. The geopotential ϕ at grid point 15 when $u_0(x)=\exp[-\sin^2(2\pi xL/l)]$, $v_0(x)=\cos(2\pi xL/l)$, and $\phi_0=1$. Numerical scheme and time step as in Fig. 3.

Equation (21) is integrated using a Galerkin spectral technique [19] with 30 modes. The stationary solutions of Eq. (21) ($u=0$, $v=F_o\phi_x$) indicate that only v can exhibit geostrophic balance. The linear analysis of Eq. (21) around the stationary solution ($u=v=0$, $\phi=1$) indicates the existence of three modes; a stationary one, in geostrophic balance, and two dispersive modes, one westward propagating and one eastward propagating, both representing pure inertia-gravity waves with period $2\pi(1+k^2R_oF_o)^{-1/2}$ (k is a wave number). To integrate Eq. (21), a fourth-order Runge-Kutta scheme with (nondimensional) time step $\delta t=10^{-2}$ is used in order to conserve the total energy E and the total geopotential $\int\phi\,dx$. Equation (21) can exhibit irregular (chaotic) behavior depending on the choice of the initial condition similar to the simplified Hamiltonian system of Sec. II. Figures 3 and 4 show two examples of the model output. Figure 3 indicates the meridional wind v as a function of time at grid point 20 when the initial conditions are $u_0(x)=\sin(6\pi xL/l)$, $v_0=\cos(6\pi xL/l)$, and $\phi_0=1$, while Fig. 4 shows the geopotential ϕ at grid point 15 when $u_0=\exp[-\sin^2(2\pi xL/l)]$, $v_0=\cos(2\pi xL/l)$, and $\phi_0=1$. Some of the behavior of the model phase space is shown in Fig. 5. It seems that for the same run, the phase space trajectory appears to be quasiperiodic in some regions [Fig. 5(b)] and irregular in others [Fig. 5(c)].

B. Synchronization in the shallow-water model

In order to obtain synchronization in the shallow-water model, Eq. (21) is integrated forward in time using a fourth-order Runge-Kutta scheme with (nondimensional) time step $\delta t=10^{-2}$ and with the same initial condition as in Fig. 4. The choice is made of this numerical scheme because it provides a way to track the synchronization with high accuracy. Other initial conditions for the control run have been used but the results concerning the synchronization rate were unaffected and we choose to concentrate on the initial condition of Fig. 4 which produces an irregular trajectory of the geopotential (Fig. 4).

The control run is saved each time step. The model is then rerun with the same time step and with initial conditions taken from the end of the control run and each $\Delta t=N\delta t$, for different values of N, we insert one (u, v, or ϕ) or two (u and ϕ, for example) model variables from the control run (driving system) in the role of the same variables of the new run (driven system). It should be noted that in practice there are no instruments that observe only one component of the wind, but only the wind speed while Doppler radars observe the radial wind component with respect to the instrument.

In Fig. 6 we show the squared error between the driving (control run) and the driven systems at times when u is inserted [Fig. 6(a)] and when v is inserted [Fig. 6(b)] for different inserting time intervals Δt corresponding to $N=50$, 100, 150, and 300. The errors are measured, for the four cases, at the same time

$$\sigma=n\Delta t=300n\,\delta t \tag{23}$$

(n is integer), that is, every $300\delta t=8.5$ h. The curves in Fig. 6 are shown with time along the x axis so with larger N fewer insertions have occurred. The decreasing errors in Fig. 6 indicate a faster convergence for larger $\Delta t\leqslant\Delta t_o$ where Δt_o is around $150\delta t$ [Fig. 6(a)] and $130\delta t$ [Fig. 6(b)] after which the synchronization (or convergence) rate decreases with further increase of Δt until eventual divergence where the systems are no longer synchronized. The errors in Fig. 6 level off at about 10^{-7}. The same behavior is observed but with a much smaller squared error when the mass field ϕ and one component (u or v) of the wind field are updated. Figure 7 shows this convergence rate when u and ϕ are updated. The

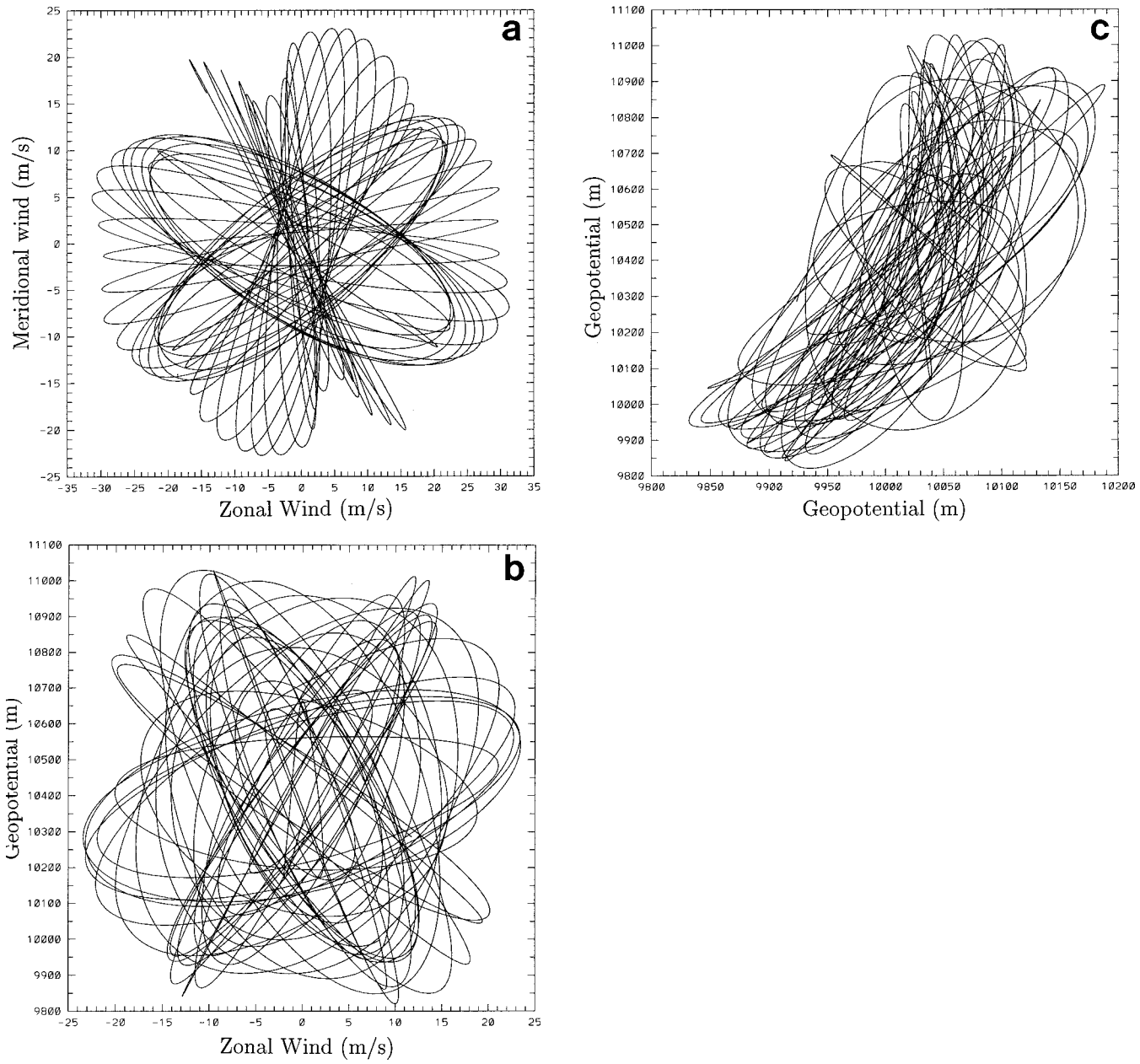

FIG. 5. Zonal wind u versus meridional wind v at grid points 27 and 10, respectively (a), geopotential ϕ versus u at the same grid point 10 (b) showing, both a regular (quasiperiodic) model phase space behavior and, ϕ at grid point 15 versus the same variable at grid point 10 indicating an irregular behavior (c). Same trajectory as in Fig. 4.

errors in this figure reach the machine accuracy where the driven system converged toward the driving system.

It is worth mentioning that since the total mass is conserved, the choice of the initial geopotential for the synchronization is crucial. For example, when the wind (one component or both) is inserted, the process cannot converge without altering the mean of the computed geopotential or including a dissipation [20]. Normally, if the numerical scheme is conservative (with no dissipation) there is no need to do so each time, but we need only get the correct total mass right at the start of the insertion experiment. Note that the previous reasoning does not apply to the energy E because this latter is a function of the whole set of model variables and there is no need for it to have the correct initial value. Note also that the systems do not synchronize when only the mass field is inserted as pointed out in [10] although we noticed at the beginning of the insertion a decrease of SQE with Δt but the error levels off very quickly and becomes constant. In this case the addition of a dissipation in the model equations can make the process converge [20].

In order to show more clearly the variation of the synchronization rate as a function of the inserting time interval Δt during the process, we report in Fig. 8 a contour plot of the logarithm of the squared error [ln(SQE)], when (u,ϕ) are inserted, as a function of Δt and the number of inserting cycles n (i.e., as the inserting process progresses with time), along with hyperbolae, $n\Delta t=\sigma$ for different values of σ. In this way there are two ways to track the convergence of the process as the inserting time interval Δt varies. One can follow the synchronization as a function of Δt for a fixed number of inserting cycles n by following a horizontal line [Eq. (18)] or by following a fixed hyperbola corresponding

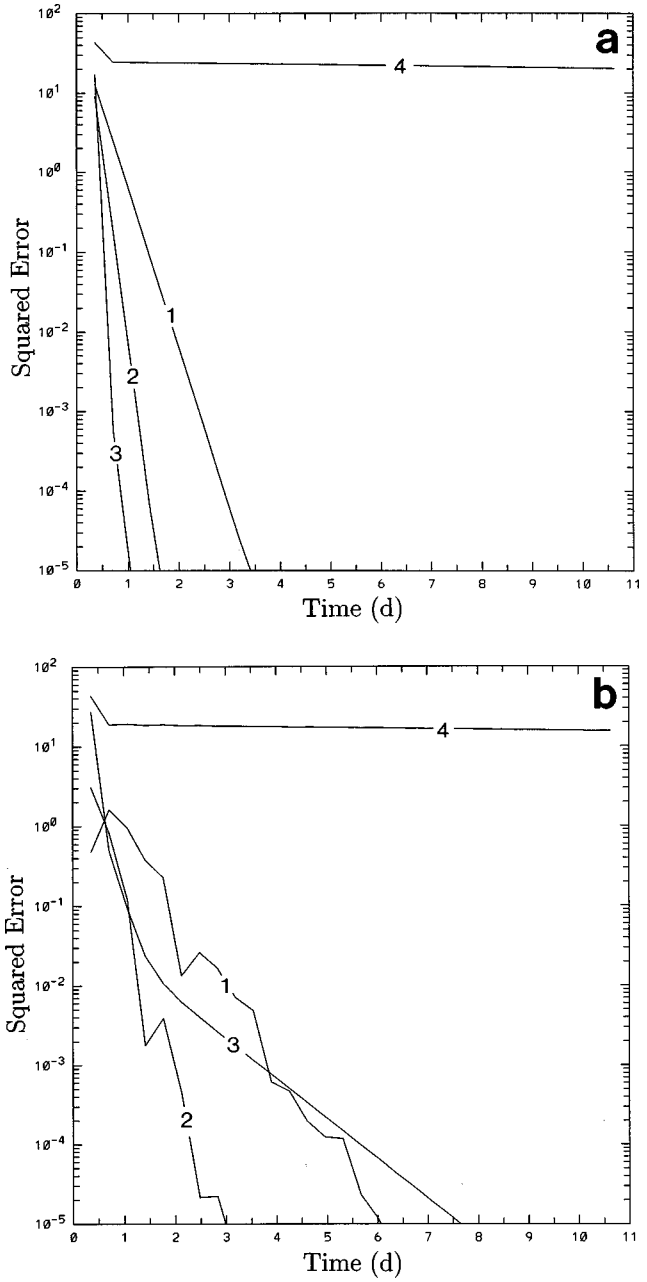

FIG. 6. The squared error vs time when u is inserted (a) and when v is inserted (b) each $50\delta t$ (curve 1), $100\delta t$ (curve 2), $150\delta t$ (curve 3), and $300\delta t$ (curve 4). The errors are taken at the same time (see text). The driving trajectory is the same as in Fig. 4.

to actual time [Eq. (19)], which is more interesting since larger Δt inserts less data. Clearly, Fig. 8 shows again that the synchronization rate increases with Δt until $\Delta t_o \approx 4.2$ h, after which the process reverses.

A similar, but not identical, synchronization can be performed by adopting two different numerical schemes for the driving and driven systems, respectively. This experiment allows for some ''noise,'' albeit small, to be included to mimic real situations. We performed experiments where the control run is integrated with a fourth-order Runge-Kutta scheme while the updating run (driven system) is integrated with a leapfrog scheme. Results from these experiments are shown in Fig. 9 where the zonal wind u is inserted, as in Fig. 6(a), each 0.5, 1, 1.5, and 3 time units. As can be seen,

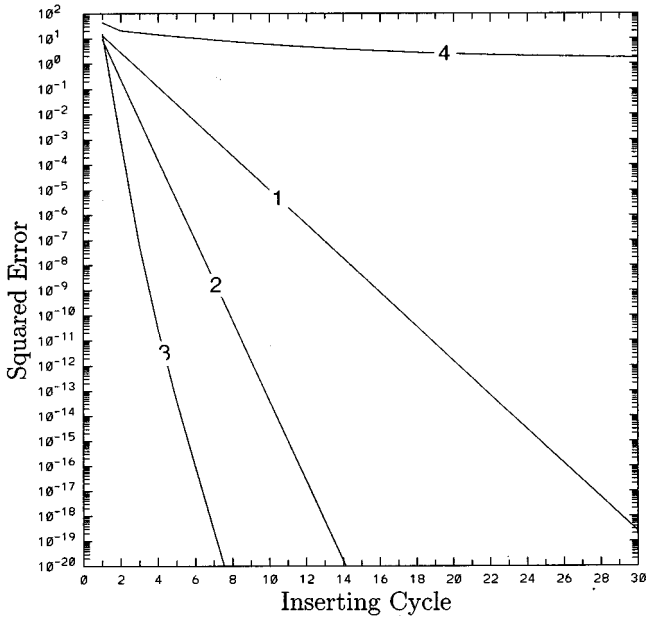

FIG. 7. Same as in Fig. 6 but when (u,ϕ) are inserted. Units on the x axis: 8.5 h.

results are quantitatively and qualitatively reproduced when compared to the case of ''perfect'' observations indicating again synchronization in agreement with [5]. However, the asymptotic value of the error is higher than the case of ''perfect'' observations, shown, for example, in Fig. 6(a), as noted by [9].

The results just presented are obtained for midlatitudes at 45 °N. It is, however, equally important to see the dependence of the optimal time interval with the position of the f plane, i.e., the latitudinal circle, although in practice the updating interval is governed by the availability of observa-

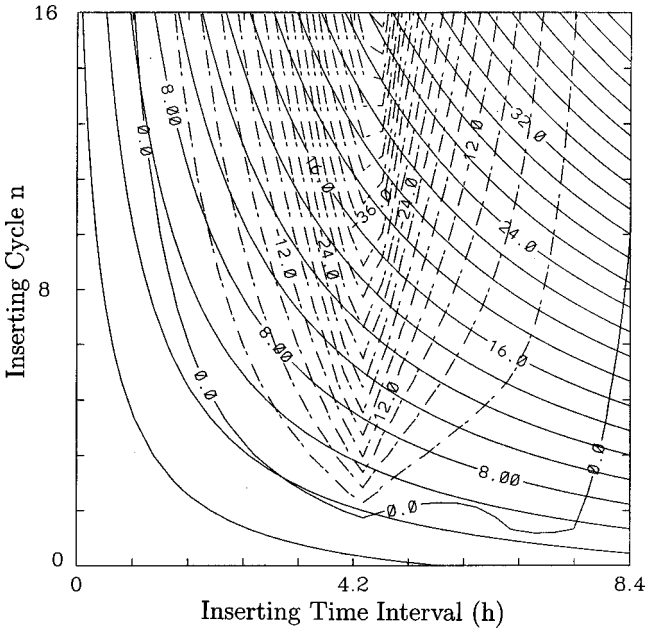

FIG. 8. Logarithm of the squared error [ln(SQE)] as a function of the inserting time interval Δt and the number of inserting cycles n when (u,ϕ) are inserted (dashed lines) and the hyperbolae $n\Delta t = \sigma$ (solid lines). Driving trajectory as in Fig. 6.

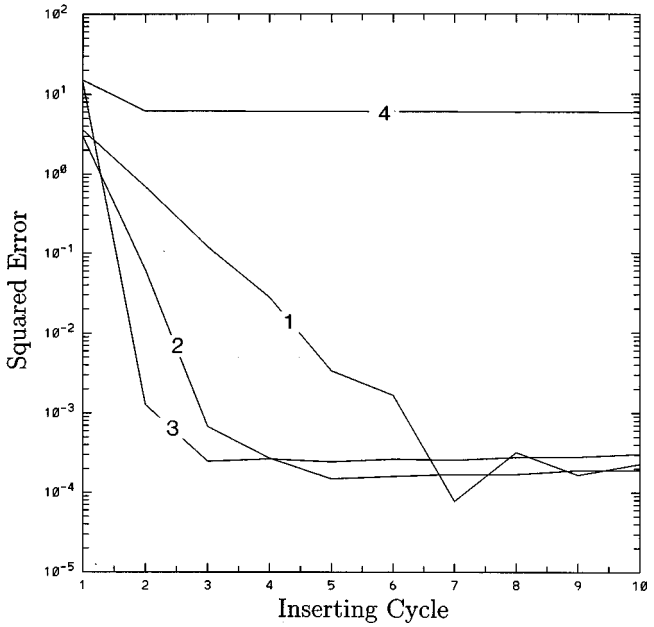

FIG. 9. Same as in Fig. 6(a) but with a fourth-order Runge-Kutta numerical scheme for the control run (driving system) and a leapfrog for the updating run (driven system). Units on the x axis as in Fig. 7 (8.5 h).

tions, but in the framework of the present context it is under our control. One reason behind this latitudinal dependence is that polar orbiting nadir sounders, satellites that measure meteorological variables like temperature and wind profiles along polar orbits, tend to sample the polar regions more frequently. Also, because most numerical models are spectral, the singularity at the poles implies that the density of grid points increases as we move poleward. The variation of the optimal inserting time interval with latitude is addressed below and will be analyzed analytically in the next section.

To study the variation of the convergence rate of the synchronization with latitude, Fig. 10(a), like Fig. 8, shows ln(SQE) when u and ϕ are inserted as a function of the inserting time interval Δt and the latitude φ. The rate of synchronization becomes faster as Δt increases up to a certain value around 1.4 time units, indicated approximately by the heavy dashed line, after which the rate reverses as Δt increases further. This observation holds especially around the midlatitudes and slightly away from the equator and the north pole. Since time is nondimensionalized by $f^{-1}=(2\Omega\sin\varphi)^{-1}$, it follows that Δt_o is around $1.4(2\Omega\sin\varphi)^{-1}$. When v and ϕ are inserted [Fig. 10(b)] the structure of the curves is slightly more complicated than that of Fig. 10(a), however, one notices that for small Δt (measured in nondimensional time units), the convergence rate is independent of latitude. In particular, Fig. 10(b) shows that Δt_o (in nondimensional time units), indicated by the heavy dashed line, behaves like a hyperbola with latitude. The heavy solid line in Fig. 10(b) will be discussed in the analytical interpretation in Sec. VI.

IV. ANALYTICAL INTERPRETATION AND VARIATION OF THE SYNCHRONIZATION RATE WITH LATITUDE

In order to analyze the convergence rate of synchronization by periodic insertion and its variation with latitude,

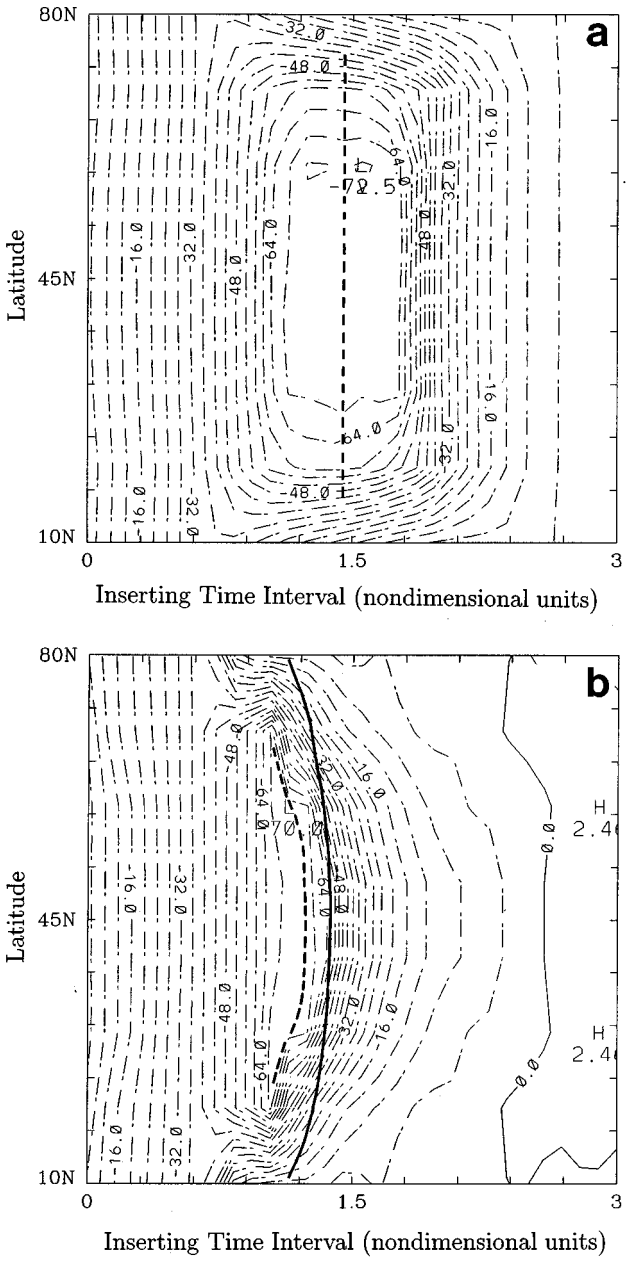

FIG. 10. Logarithm of the squared error [ln(SQE)] as a function of the inserting time interval Δt and the latitude φ when (u,ϕ) are inserted (a) and when (v,ϕ) are inserted (b). The heavy dashed lines in (a) and (b) show approximately the position of Δt_o as a function of latitude [$\approx$1.4 time units in (a)] while the heavy solid line in (b) shows the theoretical value of Eq. (30) of $\Delta t_o=\sqrt{2}(1-0.023/\sin^2 2\varphi)$. Driving trajectory as in Fig. 6.

some simplifications have to be made since it is not possible to use the full shallow-water model Eq. (21) in the manner of the analysis presented in Sec. II. In order to achieve this we start by denoting by $l=2d\pi\cos\varphi$ the circumference of the circle at latitude φ, d is the earth radius, $a=l/L$, $R=2\pi R_o/a$, and $F=2\pi F_o/a$. The model variables of Eq. (21) are expanded in Fourier series;

$$u=\sum_{m=-\infty}^{\infty} u_m(t)e^{2\pi imx/a} \tag{24}$$

for the zonal wind u and similarly for the meridional wind v and the geopotential ϕ. Obviously we have $u_{-m}(t)=u_m^*(t)$ where the superscript (*) denotes the complex conjugate. Using Eq. (24), an infinite set of ordinary differential equations can be derived from Eq. (21) which read

$$\begin{aligned}
&\dot{u}_k+iR\sum_{m+n=k} nu_mu_n+iFk\phi_k-v_k=0,\\
&\dot{v}_k+iR\sum_{m+n=k} nu_mv_n+u_k=0,\\
&\dot{\phi}_k+iR\sum_{m+n=k} (m+n)u_m\phi_n=0
\end{aligned} \tag{25}$$

for $k=\ldots,-2,-1,0,1,2,\ldots$.

For our purpose these equations are to be simplified by considering only a few modes. The first two modes, u_0 and u_1, and similarly for v and ϕ, are considered. If we denote $u_m=u_m^{(1)}+iu_m^{(2)}$, where the superscripts (1) and (2) stand, respectively, for the real and imaginary parts of the variable (u_0 is real) and remembering the fact that u_{-m} is the complex conjugate of u_m and similarly for v and ϕ, we obtain the following set of nine ordinary differential equations:

$$\begin{aligned}
\dot{u}_0&=v_0,\\
\dot{u}_1^{(1)}&=Ru_0u_1^{(2)}+F\phi_1^{(2)}+v_1^{(1)},\\
\dot{u}_1^{(2)}&=-Ru_0u_1^{(1)}-F\phi_1^{(1)}+v_1^{(2)},\\
\dot{v}_0&=2R(u_1^{(1)}v_1^{(2)}-u_1^{(2)}v_1^{(1)})-u_0,\\
\dot{v}_1^{(1)}&=Ru_0v_1^{(2)}-u_1^{(1)},\\
\dot{v}_1^{(2)}&=-Ru_0v_1^{(1)}-u_1^{(2)},\\
\dot{\phi}_0&=0,\\
\dot{\phi}_1^{(1)}&=R(\phi_0u_1^{(2)}+u_0\phi_1^{(2)}),\\
\dot{\phi}_1^{(2)}&=-R(\phi_0u_1^{(1)}+u_0\phi_1^{(1)}).
\end{aligned} \tag{26}$$

Some remarks are worth mentioning before proceeding. From Eq. (26), without loss of generality we can set ϕ_0 to 1. Equation (26) is still too complicated to be used in the manner of the Hénon and Heiles system presented in Sec. II, and some further simplifications are needed. We notice, for example, that if we drop the nonlinear terms from $\dot{v}_0$, the system becomes completely integrable and equivalent to a linear system. Since we want a nonlinear system which is simple enough to be treated, we keep the nonlinear terms in $\dot{v}_0$. To get a minimum set of nonlinear equations, we keep only one nonlinear equation for u and similarly for v by dropping the nonlinear terms from the remaining u and v tendency equations and keep unchanged the equations for ϕ tendency. After denoting $(x_1,x_2,x_3)=(u_0,u_1^{(1)},u_1^{(2)})$, $(y_1,y_2,y_3)=(v_0,v_1^{(1)},v_1^{(2)})$, and $(z_2,z_3)=(\phi_1^{(1)},\phi_1^{(2)})$ and making use of these simplifications, we derive the following eight-dimensional dynamical system:

$$\begin{aligned}
\dot{x}_1&=y_1,\\
\dot{x}_2&=Rx_1x_3+Fz_3+y_2,\\
\dot{x}_3&=-Fz_2+y_3,\\
\dot{y}_1&=2R(x_2y_3-x_3y_2)-x_1,\\
\dot{y}_2&=-x_2,\\
\dot{y}_3&=-x_3,\\
\dot{z}_2&=R(x_3+x_1z_3),\\
\dot{z}_3&=-R(x_2+x_1z_2).
\end{aligned} \tag{27}$$

We are not merely concerned about transforming Eq. (27) into a more compact form as in [21], rather we would like to keep the variables as they are so that their physical meaning remains clear for the purpose of analyzing the insertion procedure. The Jacobian of Eq. (27), and the other terms which come from the $O(\Delta t^3)$ resolvent expansion Eq. (10) are calculated in Appendix B. It is clear from Appendix B that when u and ϕ are inserted the spectral radius ρ_n of $\mathbf{A}_n$, as obtained from Eq. (10), is

$$\rho_n=\left|1-\frac{\Delta t^2}{2}\right|^n$$

and is a decreasing function of Δt for $0\leqslant\Delta t\leqslant\sqrt{2}$. Since time was nondimensionalized by f^{-1}, we have the following value for the optimum inserting time interval:

$$\Delta t_o=\frac{\sqrt{2}}{2\Omega\sin\varphi}. \tag{28}$$

Equation (28) is very close to the value found in the preceding section around the midlatitudes when the full 1D shallow-water model Eq. (21) was used for synchronization. Of course, close to the equator, the equations have to be modified and a β-plane model would certainly be a better choice but it is not addressed here. Notice that we analyzed the case when both u and ϕ are inserted together because in this case the number of the remaining variables, and also the dimension of the amplification matrix, are reduced. In addition, because in this case the errors are small enough, it is easier to follow the detailed behavior of the convergence rate during synchronization.

When only one variable is inserted, the amplification matrix is too complicated to be treated easily. Even when we insert v and ϕ, the amplification matrix is not simple (for example, triangular) as we may wish it to be, like the case where u and ϕ are inserted. This is due to the lack of symmetry in the 1D shallow-water equations because the advection is carried only by the zonal wind. In order to analyze this latter case, we are obliged to drop the nonlinear terms from $\dot{x}_2$ and consider an approximation to the amplification matrix for this case, as indicated in Appendix B. The eigenvalues of the triangular matrix are $(1-\Delta t^2/2)$ and $[1-(1+RF)\Delta t^2/2]$, and its spectral radius therefore depends on the size of Δt. As pointed out in Appendix B, for a given small Δt the spectral radius ρ_n (or rate of synchronization) is

$|1-\Delta t^2/2|^n$ and is independent of latitude (nondimensional Δt) as shown in Fig. 10(b). However, for larger Δt we have

$$\rho_n = \left| 1-(1+RF)\frac{\Delta t^2}{2} \right|^n . \tag{29}$$

If we consider this latter expression, the value of Δt_o is given by $\sqrt{2}(1+RF)^{-1/2}$. Since RF is small compared to 1, the nondimensional interval Δt_o becomes approximately equal to (Appendix B)

$$\Delta t_o = \sqrt{2}\left(1-\frac{\Phi_0}{2d^2\Omega^2 \sin^2 2\varphi} \right). \tag{30}$$

Considering the value of Φ_0 used in the text, Eq. (30) becomes

$$\Delta t_o \approx \frac{\sqrt{2}}{2\Omega \sin\varphi}\left(1-\frac{0.023}{\sin^2 2\varphi} \right) \tag{31}$$

in dimensional time. The hyperbola Eq. (30) is shown in Fig. 10(b) by the heavy solid line. Although the experimental curve (heavy dashed line) is slightly shifted away from the theoretical one, they look very similar, particularly around the midlatitudes where they would fit very well if they were put on top of each other. This shift is certainly due to the large simplifications applied to obtain Eq. (30) and a small correction accounting for these simplifications can be added if we want a very accurate formula.

V. COMPARISON WITH THE LINEARIZED MODEL

The study presented in the previous sections is based on the full nonlinear 1D shallow-water model equations. The natural question which then arises is how much we gain if we use the linearized model to explain the observed behavior of the synchronization in the nonlinear system. As shown below, the linearized model can explain this behavior if the ''right'' stationary state is chosen. It is certainly true that as far as chaotic synchronization is concerned linear models are not a good choice, nonetheless these models can be useful since during an updating procedure the nonlinear dynamical system is perturbed, therefore the linearized model arises naturally.

We consider a linearized version of Eq. (21) about a state of rest with the nondimensional geopotential $\phi=1$ which reads

$$\begin{aligned} u_t + F_o\phi_x - v &= 0, \\ v_t + u &= 0, \\ \phi_t + R_o u_x &= 0. \end{aligned} \tag{32}$$

In terms of Fourier modes, we obtain for mode k the linear ordinary differential equation

$$\hat{\mathbf{V}}_t = \mathbf{A}\hat{\mathbf{V}}, \tag{33}$$

where $\hat{\mathbf{V}}=(\hat{u},\hat{v},\hat{\phi})^T$ where $\hat{u}$, $\hat{v}$, and $\hat{\phi}$ are the components of u, v, and ϕ, respectively, along the Fourier mode k, and

$$\mathbf{A} = \begin{pmatrix} 0 & 1 & ikF \\ -1 & 0 & 0 \\ ikR & 0 & 0 \end{pmatrix}.$$

An initial error $\boldsymbol{\eta}(0)$ superimposed upon $\hat{\mathbf{V}}$ at time $t=0$ will evolve after Δt as

$$\boldsymbol{\eta}(\Delta t) = e^{\mathbf{A}\Delta t}\boldsymbol{\eta}(0) = \mathbf{R}(\Delta t)\,\boldsymbol{\eta}(0), \tag{34}$$

where the propagator $\mathbf{R}(t)$ is given by

$$\mathbf{R}(t) = \begin{pmatrix} \cos\omega t & \dfrac{\sin\omega t}{\omega} & \dfrac{ikF}{\omega}\sin\omega t \\ -\dfrac{\sin\omega t}{\omega} & 1-\dfrac{1}{\omega^2}(1-\cos\omega t) & -\dfrac{ikF}{\omega^2}(1-\cos\omega t) \\ \dfrac{ikR}{\omega}\sin\omega t & \dfrac{ikR}{\omega^2}(1-\cos\omega t) & \dfrac{1}{\omega^2}+\left(1-\dfrac{1}{\omega^2}\right)\cos\omega t \end{pmatrix}. \tag{35}$$

In Eq. (35) ω is the inertio-gravity wave frequency given by $\omega^2 = 1+k^2RF$. Equation (32) or Eq. (33) can also be written in terms of vorticity ζ and divergence D. It can be seen that the (ζ,D) version [10,20], and Eq. (32), have the same frequencies (eigenvalues) and only the off-diagonal elements of their respective propagators are different. It is also worth noting that the (ζ,D) version of the linearized Eqs. (32) is not different from that of the 2D linearized equations. This point is important, in this regard, because it means that results from this section are also valid for the 2D shallow-water model which contains different dynamical time scales.

In what follows and unless otherwise stated, we shall only discuss the cases when two model variables out of three are updated, i.e., perfectly known. The propagator Eq. (35), as it stands, does not explain the observed behavior of the insertion procedure but for small Δt Taylor expansion of the resolvent in Eq. (34) shows that the crossover point, Δt_o, from the preceding section can be recovered (when we restrict ourselves to small k). This shows that the observed convergence behavior in the nonlinear model is mainly controlled by the first few modes, i.e., large scales.

In order to use the linear system, like Eq. (32), for this purpose a stationary state is required to linearize about. The choice of this state is important. In fact, consider the Hamil-

tonian system of Sec. II, linearized about one singular point, along with the expansion of the exponential propagator. By examining Eqs. (14)–(16), it turns out that if the singular point is chosen to be $(\pm\sqrt{3}/2, -\frac{1}{2}, 0, 0)$ or (0, 1, 0, 0), then clearly the linearized system cannot explain the convergence behavior in the nonlinear system. However, when the singular point is chosen to be the origin then the linearized system can provide the right explanation of the previous behavior and gives correct estimates of the optimum time interval Δt_o.

Due to the dynamical structure of the Hamiltonian system of Sec. II, the time average of the system trajectory is close to the origin [11]. The climatology of the shallow-water model (see Fig. 5) is also close to the stationary state used to obtain the linearized system in Eq. (32). Hence, in order to provide a robust explanation of the convergence behavior during the synchronization by direct insertion in more complicated geophysical systems, we conjecture that the best stationary states to be used for the linearization are those closest to the climatology. These (quasi) stationary states are generally referred to as weather or flow regimes [22]. In the atmosphere such flow regimes have been observed and have been noticed to persist for several weeks [23]. The question of the existence of (quasi) stationary states close to the climatology has been addressed theoretically using simple barotropic vorticity equation as well as atmospheric general circulation models [24].

These states play a crucial role in the predictability of the atmospheric flow and it should not be surprising to find that the optimum inserting time interval can be linked to these states and to the climatology. The importance of the climatology in this regard can be noted from Eqs. (A3) and (A4), in the Hamiltonian system, for example, relating the rate of convergence during the synchronization process to the mean state. In many instances, it is practical to just replace the stationary state by the climatology although it is not a (quasi) stationary state. The climatology can be approximated by the time average of the model output over a long time period although a rigorous analytic determination of it from the model equations is generally hopeless [25]. Linearization of the flow around the climatology has long been used in other contexts to study, for example, the stability of the mean flow in order to provide explanations of the dynamical processes responsible for the generation and maintenance of atmospheric variability [26].

VI. SUMMARY AND CONCLUSION

We have investigated the rate, or speed, of synchronization by direct insertion as a function of the inserting time interval. The question has been first addressed theoretically within a simplified Hamiltonian system. This choice has been made for two basic reasons. First, the chosen system is simple enough to be treated analytically but also complicated enough, due to its dynamical properties being similar to real systems. Second and foremost, geophysical systems are basically Hamiltonian, especially when dissipation and forcing are weak. It is shown that up to a certain limit Δt_o, that we termed the optimum time interval, the synchronization rate increases as the inserting time interval increases. Beyond this optimum interval the synchronization rate decreases with further increase of the inserting time interval until the process eventually diverges, i.e., the driving and driven systems no longer synchronize.

This crossover point has been correctly predicted by the theory using a second-order Taylor expansion of the system resolvent. We then applied it to a simplified version of the primitive equations, that is, a 1D nonlinear spectral shallow-water model over a periodic domain around 45 °N. We find that when the zonal wind is inserted, the optimum inserting time interval is around 4 h while it is slightly less when the meridional wind is inserted. It is worth mentioning, although this has not been explicitly addressed, that the $O(\Delta t^2)$ Taylor expansion of the resolvent can also predict the upper limit of Δt where the procedure is likely to diverge. Although the 1D shallow-water model is restrictive, the analyzed behavior of the convergence rate of direct insertion still holds for more realistic models at least qualitatively. The fact that the model is dominated mainly by inertio-gravity modes is perhaps the reason why the optimum time interval is smaller than the 12 h period suggested in [7].

We then focused on the variation of the synchronization rate and the optimum time interval with latitude within the previous 1D shallow-water model Eq. (21). This question has been brought up because the temporal and spatial resolutions of several observing systems and of most numerical prediction models, respectively, are coarser equatorward. It is found, in particular, that the optimum inserting time interval varies as the inverse of the Coriolis parameter, meaning that we should insert, or update, more frequently as we move poleward. This rule is mostly valid around the midlatitudes where the inverse of the Coriolis parameter does not vary considerably.

A simplified low-order dynamical system is derived from the 1D shallow-water model by discarding some of the nonlinear terms rather in the manner of [21]. This experiment was aimed at building a simple nonlinear dynamical system to help put the experimental results in an analytical framework. An approximation to the optimum time interval Δt_o is found to be $\sqrt{2}/(2\Omega \sin\varphi)$ when (u, ϕ) are inserted. A slightly different formula is found when (v, ϕ) are inserted, and it is shown that these formulas fit quite well with the experimental results drawn from the nonlinear shallow-water model.

In order to check whether the previous results can be explained using a linear model, a linearized system derived from the shallow-water model is introduced and an analysis of the dependence of the synchronization on the inserting time interval performed. It turns out that the linearized model is able to explain the convergence behavior of the insertion procedure and allows estimation of the crossover point Δt_o through the use of an $O(\Delta t^2)$ Taylor expansion of the resolvent operator, which is simply an exponential matrix. This is promising because it is possible to use linear versions of more complicated nonlinear systems to calculate their propagators, which have simple forms, and then estimate the crossover point using a second-order Taylor expansion. The only point which needs to be addressed is the choice of the (quasi) stationary state about which to linearize the model. It is suggested that the closest (quasi) stationary state to the climatology, or for practical purposes, the climatology itself, can be used in this regard.

Our results shed some light on the importance of the inserting time interval in synchronization. Several points, however, remain to be investigated. The main point is the extension of these results to more realistic models like a 2D primitive equation model where several time scales are present. The question of dissipation has not been explicitly addressed, however, experiments performed with the addition of dissipation show that the results found previously are quite robust to small dissipation and/or forcing [11]. The same robustness is also observed when two different numerical schemes (fourth-order Runge-Kutta or leapfrog) are used for the driving (control run) and the driven systems, respectively, or vice versa, to mimic real situations in which observations are usually contaminated with noise although, in the presence of realistic noise level, other techniques like Kalman filtering [27] or variational adjustment [28] can be used.

ACKNOWLEDGMENTS

This work was partially supported by EC Environment Project No. AGORA CT95-0113 and, at a later stage, by UGAMP. The author wishes to thank Dr. K. Haines for beneficial discussions and for reading the manuscript, and Professor B. Harwood for helpful comments on the paper.

APPENDIX A: ON THE LIMITING BEHAVIOR OF THE SPECTRAL RADIUS OF THE AMPLIFICATION MATRIX

We consider the amplification matrix given by Eq. (16) obtained when (y,p) are inserted. In the meantime it should be noted that at $O(\Delta t^4)$, the situation corresponding to the insertion of (x,y) can be shown to be an application of the simpler case corresponding to the insertion of (y,p) which is presented below. In order to analyze the spectral radius $\rho_n = \rho(\mathbf{A}_n)$, $\mathbf{A}_n = \Pi_{k=1}^{n} \mathbf{R}_{uu}^{(n-k+1)}$, we analyze the two products $\rho_n^{\pm}$ appearing in Eq. (17). For small Δt^2 we have

$$\ln \rho_n^{\pm} = \sum_{k=1}^{n} -\frac{\Delta t^2}{2}(1 \pm 2y_k) + O(\Delta t^4) = -n\frac{\Delta t^2}{2}(1 \pm 2\overline{y_n}) + O(\Delta t^4), \tag{A1}$$

where $\overline{y_n} = (1/n)\Sigma_{k=1}^{n} y_k$ is an average of the variable y from the trajectory. For n large enough, $\overline{y_n}$ is approximately equal to the climate $\overline{y}$ of the variable y (independent of Δt because of the regular or stochastic character of the trajectories) so that at $O(\Delta t^4)$ we have

$$\ln \rho_n \sim -n\frac{\Delta t^2}{2}(1 - 2|\overline{y}|). \tag{A2}$$

We notice first that the variable y belongs to $[-1/2, 1]$ for the bounded motion (i.e., bounded U) which guarantees the convergence of $\overline{y_n}$ towards $\overline{y}$ as n tends to infinity. It can also be shown [11] that $1 - 2\overline{y} \geqslant 0$, implying that $|\overline{y}| \leqslant \frac{1}{2}$, as required for convergence, i.e., $\rho_n \to 0$ when $n \to \infty$. It is then clear from Eq. (A2) that for large n, ρ_n is a decreasing function of (small) Δt for $\Delta t \leqslant \Delta t_o$. It also shows that $\rho_{n_2}(\Delta_2 t) \leqslant \rho_{n_1}(\Delta_1 t)$ for $n_2 \leqslant n_1$ for which $n_1 \Delta_1 t = n_2 \Delta_2 t$. Furthermore, Eq. (A2) tells us that the spectral radius behaves, for large n, to accuracy $O(\Delta t^4)$ as

$$\rho_n \sim \left| 1 - \frac{\Delta t^2}{2}(1 - 2|\overline{y}|) \right|^n. \tag{A3}$$

The optimal time interval is then defined as the one which minimizes the estimated spectral radius. Equation (A3) gives an approximation to the optimal time interval Δt_o after which ρ_n increases with Δt. We have

$$\Delta t_o = \frac{\sqrt{2}}{\sqrt{1 - 2|\overline{y}|}} \sim \sqrt{2}(1 + |\overline{y}|), \tag{A4}$$

which is very close to $\sqrt{2}$ ($\overline{y}$ is generally very close to zero). Finally, we only note that it is also possible to derive from Eq. (A3) an approximation to the lower bound on Δt after which the process may diverge [11].

APPENDIX B: ANALYSES FOR THE SHALLOW-WATER MODEL

We consider the simplified dynamical system Eq. (27) whose Jacobian $\mathbf{F}'$ is given by

$$\mathbf{F}'(\mathbf{X}(t)) = \begin{pmatrix} 0 & 0 & 0 & 1 & 0 & 0 & 0 & 0 \\ Rx_3 & 0 & Rx_1 & 0 & 1 & 0 & 0 & F \\ 0 & 0 & 0 & 0 & 0 & 1 & -F & 0 \\ -1 & 2Ry_3 & -2Ry_2 & 0 & -2Rx_3 & 2Rx_2 & 0 & 0 \\ 0 & -1 & 0 & 0 & 0 & 0 & 0 & 0 \\ 0 & 0 & -1 & 0 & 0 & 0 & 0 & 0 \\ Rz_3 & 0 & R & 0 & 0 & 0 & 0 & Rx_1 \\ -Rz_2 & -R & 0 & 0 & 0 & 0 & -Rx_1 & 0 \end{pmatrix}. \tag{B1}$$

The operator $\mathbf{F}'^2(\mathbf{X}(t))$ is then given by

$$-\begin{pmatrix} 1 & -2Ry_3 & 2Ry_2 & 0 & 2Rx_3 & -2Rx_2 & 0 & 0 \\ RFz_2 & 1+RF & 0 & -Rx_3 & 0 & -Rx_1 & 2RFx_1 & 0 \\ RFz_3 & 0 & 1+RF & 0 & 0 & 0 & 0 & RFx_1 \\ -2R^2x_3y_3 & -2Rx_3 & 2R(x_2-Rx_1y_3) & 1 & -2Ry_3 & 2Ry_2 & -2RFy_2 & -2RFy_3 \\ Rx_3 & 0 & Rx_1 & 0 & 1 & 0 & 0 & F \\ 0 & 0 & 0 & 0 & 0 & 1 & -F & 0 \\ R^2x_1z_2 & R^2x_1 & 0 & -Rz_3 & 0 & -R & RF+R^2x_1^2 & 0 \\ R^2(x_3+x_1z_3) & 0 & 2R^2x_1 & Rz_2 & R & 0 & 0 & RF+R^2x_1^2 \end{pmatrix} \tag{B2}$$

while $\dot{\mathbf{F}}'(\mathbf{X}(t))$ can be derived simply by time differentiating the elements of the Jacobian $\mathbf{F}'(\mathbf{X}(t))$. The $O(\Delta t^2)$ expression of the resolvent is then obtained from Eq. (10) using Eqs. (B1) and (B2). It can be seen from Eq. (B1) that when the zonal wind and the geopotential (u,ϕ) [that is, (x_1,x_2,x_3,z_2,z_3)] are inserted, the amplification matrix given by Eq. (10) becomes

$$\mathbf{R}_{uu}^{(k)}=\begin{pmatrix} 1-\dfrac{\Delta t^2}{2} & R(-2x_3(t_k)+Fz_2(t_k)\Delta t)\Delta t & R(2x_2(t_k)+[Fz_3(t_k)+Rx_1(t_k)x_3(t_k)]\Delta t)\Delta t \\ 0 & 1-\dfrac{\Delta t^2}{2} & 0 \\ 0 & 0 & 1-\dfrac{\Delta t^2}{2} \end{pmatrix}. \tag{B3}$$

Equation (B3) shows that for $\Delta t<\sqrt{2}$, the convergence is faster for larger Δt from which Eq. (28) is derived. The expression of $\mathbf{R}_{uu}^{(k)}$ Eq. (B3) can also provide an upper limit on Δt above which convergence may cease.

When (v,ϕ) are inserted $\mathbf{R}_{uu}^{(k)}$ becomes

$$\mathbf{R}_{uu}^{(k)}=\begin{pmatrix} 1-\dfrac{\Delta t^2}{2} & Ry_3(t_k)\Delta t^2 & -Ry_2(t_k)\Delta t^2 \\ R(x_3(t_k)+[\frac{1}{2}y_3(t_k)-Fz_2(t_k)]\Delta t)\Delta t & 1-(1+RF)\dfrac{\Delta t^2}{2} & R\left(x_1(t_k)+y_1(t_k)\dfrac{\Delta t}{2}\right)\Delta t \\ -RFz_3(t_k)\dfrac{\Delta t^2}{2} & 0 & 1-(1+RF)\dfrac{\Delta t^2}{2} \end{pmatrix}. \tag{B4}$$

The form of Eq. (B4) does not explicitly allow an analytical study of the convergence as performed previously, and it would be helpful if we could get a similar expression to that obtained when (u,ϕ) is inserted. For this reason, the nonlinear term from $\dot{x}_2$ in Eq. (27) is dropped, and, since the model variables z_2,z_3 are small because they are wave perturbations to $z_0=1$, the terms RFz_2 and RFz_3 are neglected from Eq. (B4) (because R and F are also small). With these large simplifications we end up with the following amplification matrix:

$$\mathbf{R}_{uu}^{(k)}=\begin{pmatrix} 1-\dfrac{\Delta t^2}{2} & Ry_3(t_k)\Delta t^2 & -Ry_2(t_k)\Delta t^2 \\ 0 & 1-(1+RF)\dfrac{\Delta t^2}{2} & 0 \\ 0 & 0 & 1-(1+RF)\dfrac{\Delta t^2}{2} \end{pmatrix}. \tag{B5}$$

This has similar structure to Eq. (B3) with similar eigenvalues except that a new term, RF, appears in the eigenvalues of Eq. (B5) due to the continuity equation which involves only u. In Eq. (B5) we have two eigenvalues, however, for small Δt, the spectral radius ρ_n is $(1-\Delta t^2/2)^n$ and then the convergence rate is independent of the latitude for fixed (nondimensional) Δt to accuracy $O(\Delta t^3)$. But for larger Δt the spectral radius $\rho_n=|1-(1+RF)\Delta t^2/2|^n$, for which the optimum interval is

$$\Delta t_o=\sqrt{2}(1+RF)^{-1/2}\approx\sqrt{2}(1-\tfrac{1}{2}RF), \tag{B6}$$

with $RF=\Phi_0/d^2\Omega^2\sin^2 2\varphi$. For the value of Φ_0 chosen in the text, the preceding expression becomes $\Delta t_o\approx\sqrt{2}(1-0.023/\sin^2 2\varphi)$.

[1] L. M. Pecora and T. L. Caroll, Phys. Rev. Lett. **64**, 821 (1990); Phys. Rev. A **44**, 2374 (1991).
[2] H. Fujisaka and T. Yamada, Prog. Theor. Phys. **69**, 32 (1983).
[3] P. So, E. Ott, and W. P. Dayawansa, Phys. Lett. A **176**, 421 (1993).
[4] T. L. Caroll and L. M. Pecora, Physica D **67**, 126 (1993); K. M. Cuomo and A. V. Oppenheim, Phys. Rev. Lett. **71**, 65 (1993).
[5] R. Brown, N. F. Rulkov, and N. B. Tuffilaro, Phys. Lett. A **196**, 201 (1994); Phys. Rev. E **50**, 4488 (1994).
[6] G. S. Duane, Phys. Rev. E **56**, 6475 (1997).
[7] J. Charney, M. Halem, and R. Jastrow, J. Atmos. Sci. **26**, 1160 (1969).
[8] D. Williamson and A. Kasahara, J. Atmos. Sci. **28**, 1313 (1971); D. Williamson and R. E. Dickinson, *ibid.* **29**, 190 (1972).
[9] W. Blumen, J. Atmos. Sci. **32**, 274 (1975); **33**, 170 (1976).
[10] O. Talagrand, Tellus **33**, 43 (1981).
[11] A. Hannachi and K. Haines, Tellus, Ser. A **50**, 58 (1998).
[12] A. J. Lichtenberg and M. A. Lieberman, *Regular and Stochastic Motion* (Springer-Verlag, Berlin, 1983).
[13] T. G. Shepherd, Adv. Geophys. **32**, 287 (1990).
[14] M. Hénon and C. Heiles, Astron. J. **69**, 73 (1964).
[15] A. E. Gill, Q. J. R. Meteorol. Soc. **106**, 447 (1980); P. J. Webster, J. Atmos. Sci. **38**, 554 (1981).
[16] M. A. Cane and E. S. Sarachik, J. Mar. Res. **39**, 651 (1981); S. G. H. Philander, T. Yamagata, and R. C. Pacanowski, J. Atmos. Sci. **41**, 604 (1984); C. Wang and R. H. Weisberg, J. Clim. **9**, 3132 (1996).
[17] G. J. Haltiner and R. T. Williams, *Numerical Prediction and Dynamic Meteorology* (Wiley, New York, 1980).
[18] Y. K. Sasaki (unpublished).
[19] C. Canuto, M. Y. Hussaini, A. Quarteroni, and T. A. Zang, *Spectral Methods in Fluid Dynamics* (Springer-Verlag, Berlin, 1988).
[20] G. L. Browning and H.-O. Kreiss, J. Atmos. Sci. **53**, 335 (1996).
[21] E. N. Lorenz, J. Atmos. Sci. **43**, 1547 (1986); O. Bokhove and T. G. Shepherd, *ibid.* **53**, 277 (1996).
[22] J. G. Charney and J. G. DeVore, J. Atmos. Sci. **36**, 1205 (1979).
[23] J. Namias, J. Meteorol. **7**, 130 (1950); D. Rex, Tellus **2**, 196 (1950); J. Namias, *ibid.* **16**, 94 (1964); F. Molteni, S. Tibaldi, and T. Palmer, Q. J. R. Meteorol. Soc. **116**, 31 (1990).
[24] G. Branstator and J. D. Opsteegh, J. Atmos. Sci. **46**, 1799 (1989); K. Haines and A. Hannachi, *ibid.* **52**, 2444 (1995); A. Hannachi, J. Clim. **10**, 1357 (1997).
[25] E. N. Lorenz, Tellus **16**, 1 (1964).
[26] D. G. Andrews, Q. J. R. Meteorol. Soc. **110**, 657 (1984); A. J. Simmons, J. M. Wallace, and G. W. Branstator, J. Atmos. Sci. **40**, 1363 (1983).
[27] A. H. Jazwinski, *Stochastic Processes and Filtering* (Academic, New York, 1970); B. D. Anderson and J. B. Moore, *Optimal Filtering* (Prentice-Hall, Englewood Cliffs, NJ, 1979).
[28] J. M. Lewis and J. C. Derber, Tellus, Ser. A **37**, 309 (1985).